Pol. J. Environ. Stud. Vol. XX, No. X (XXXX), 1-14

DOI: *10.15244/pjoes/222176* ONLINE PUBLICATION DATE: 2026-09-21

Original Research

Study on Wave Characteristics in the Offshore Area of Qingdao

Bo Yu[1, 2], Ruidi Ma[1, 2], Chengzhen Ji[1, 2], Fan Jiang[1, 2]*, Bo Lu[2], Yong Ge[2], Jingyi Sun[2], Chenxu Wang[1, 2], Wei Hu[2]

[1]Key Laboratory of Ecological Prewarning, Protection and Restoration of Bohai Sea, Ministry of Natural Resources, Qingdao 266000, China

[2]North China Sea Marine Forecasting and Hazard Mitigation Center, Ministry of Natural Resources, Qingdao 266000, China

Received: 28 February 2026

Accepted: 18 May 2026

Abstract

Statistical and spectral analyses of wave characteristics in the offshore region of Qingdao are presented based on one year of continuous field observations. The intra-annual variations of significant wave height (H_s) and wave period, together with their probabilistic distributions and spectral structures, are systematically examined. H_s ranges from 0.11 to 2.78 m, with an annual mean of 0.51 m, exhibiting pronounced seasonal variability. Both wave height and wave period distributions are well represented by a two-parameter Weibull model. Spectral analysis indicates that monthly averaged wave spectra are predominantly unimodal, with peak frequencies concentrated between 0.1 and 0.2 Hz, reflecting wind-sea-dominated conditions. Bimodal spectra, indicative of mixed swell and wind-sea systems, are observed in February, August, and September. Regression analysis among characteristic wave parameters and spectral moments reveals strong correlations, while empirical ratios deviate from classical deep-water theoretical values due to shallow-water influences and mixed sea states. During Typhoon Bavi, wave spectra were predominantly single-peaked, and the wave field was dominated by low-frequency swells around 0.09 Hz. These findings provide region-specific insight into the local wave climate and offer a scientific basis for offshore engineering design and coastal hazard mitigation in the Qingdao waters.

Keywords: Qingdao offshore, wave statistics, distribution features, spectral analysis, typhoon

Introduction

The study region of Qingdao is situated in the southeastern part of Shandong Province, featuring numerous bays and a highly indented coastline with a total length of 905.2 kilometers. The region is characterized by a distinct temperate monsoon climate: summers are influenced by southeasterly monsoons, while winters are dominated by northwesterly monsoons. Additionally, the region is frequently impacted by extreme weather events such as typhoons and cold surges. In the context of increasing anthropogenic activities and climate variability, recent comprehensive assessments have emphasized the increasing variability and regional

*e-mail: oceanbuoy_bh@163.com

Tel.: +86-13512437411

0000-0002-9614-0520

differentiation of tropical cyclone activity and associated ocean wave extremes under climate change [1-3]. Wave-induced coastal erosion, infrastructure vulnerability, and ecological consequences have therefore drawn considerable scientific attention. A comprehensive understanding of wave characteristics based on field observations is essential for effective coastal management, marine hazard mitigation, and offshore engineering design in this region.

Recent advancements in marine observational technologies and third-generation numerical spectral wave models, such as the Simulating Waves Nearshore (SWAN) [4-6] and WAVEWATCH III models [7-9], have significantly enhanced our capacity to analyse wave behaviours in global and regional coastal systems. Long-term spectral hindcast simulations have provided improved insight into regional wave climate variability and spectral evolution characteristics in the South China Sea and adjacent marginal seas. Numerous studies have contributed to the understanding of wave characteristics across different climatic and geographic settings. Vandever et al. [10] examined relationships between wave height parameters and spectral width (ν) based on multi-station observations in coastal-estuarine systems. Recent updates in design-wave estimation systems based on long-term numerical model data have improved engineering-oriented wave statistics along the Korean coast [11]. In monsoon-dominated basins, recent basin-scale analyses have demonstrated that seasonal variability of wave spectra is closely linked to large-scale climate modes such as the Indian Ocean Dipole, while spectral partitioning techniques further highlight systematic differences between wind-sea and swell components across the Indian Ocean [12, 13]. Measurements and spectral reconstructions in the Arabian Sea and Bay of Bengal indicate that wave spectra frequently exhibit unimodal or bimodal structures, depending on the relative dominance and directional alignment of wind-sea and swell components under varying forcing conditions [14, 15]. Process-oriented analyses further demonstrate that strong monsoonal winds and tropical cyclones can substantially enhance significant wave height and redistribute spectral energy, leading to pronounced shifts in spectral shape and peak characteristics. For typhoon conditions, spectral analyses of northwest Pacific typhoon waves have demonstrated clear coexistence of wind-sea and swell systems, with spectral characteristics strongly dependent on storm track, intensity, and evolution stage [16-18]. These findings highlight the importance of spectral-based approaches for diagnosing mixed sea states under extreme weather systems.

Long-term in situ observations combined with numerical simulations have substantially advanced regional assessments of wave climate and extreme sea states in the Chinese marginal seas. Recent analyses based on multi-year measurements in the Bohai Sea reveal pronounced spatial heterogeneity and increasing variability of storm-driven wave conditions along the nearshore zone [19]. Field observations in semi-enclosed bays further demonstrate that local bathymetry and wind alignment strongly influence wave statistics and spectral distribution patterns [20]. Process-oriented investigations indicate that wave–current interactions can significantly modify wave parameters and spectral characteristics, particularly in coastal environments influenced by complex circulation systems [21]. In the Qingdao coastal region, coupled tide–surge–wave simulations show that extreme wave conditions are highly sensitive to typhoon intensity and background sea-level variations, with marked differences between open coasts and bay areas [22]. In the South Yellow Sea, numerical modeling suggests that radial sand ridge systems can amplify significant wave heights and alter wave evolution under extreme weather events [23]. High-resolution simulations further provide regional contrasts of mean and extreme wave climates across the Bohai, Yellow, and East China seas, highlighting spatially differentiated responses to climate forcing [24]. Observational and modeling studies indicate that tropical cyclone dynamics strongly modulate spectral peak characteristics and wave energy redistribution, with spatial contrasts between swell-dominated regions away from the storm core and wind-sea-dominated areas near the maximum wind zone [25, 26]. In semi-enclosed coastal environments, tidal modulation, local bathymetry, and limited swell penetration collectively shape wave energy distribution and spectral structure, emphasizing the importance of explicitly accounting for mixed sea states in coastal hazard assessment and wave prediction [27, 28].

Despite these advances, in situ observational data describing wave distribution, spectral characteristics, and typhoon-affected processes in the offshore region of Qingdao remain limited. This scarcity poses a barrier to the development of a comprehensive and region-specific understanding of local wave dynamics. Based on one full year of continuous wave measurements, this study focuses on: (1) intra-annual variations in significant wave height and wave period; (2) parametric modeling of the joint statistical distribution of wave height and period; (3) empirical characterization of relationships among key spectral parameters; and (4) wave processes during typhoon events. By integrating temporal wave behaviour with underlying spectral evolution mechanisms, this study establishes region-specific wave climate benchmarks that are essential for enhancing the predictive accuracy of extreme wave events and supporting the development of more resilient coastal infrastructure in the offshore environment of Qingdao.

Materials and Methods

Data

Wave parameters and spectra were measured using an Aanderaa Motus wave sensor mounted on a 1.75-meter diameter buoy. The sensor operated at a 4 Hz sampling frequency with spectral resolution covering wave periods of 1.42-30 s. The observation site was located in the Qingdao coastal waters (Fig. 1), approximately 2 km offshore at a water depth of 25 m. Continuous measurements were recorded at 30-min intervals from March 1, 2020, to February 28, 2021, yielding a complete annual dataset. Wind speed was measured at 10 m above the sea surface by a co-located meteorological buoy positioned approximately 50 m north of the wave buoy, and the sampling frequency was 1 hour.

Data quality control was conducted according to the Technical Specification for Delayed-Mode Ocean Observation Data Quality Control and Check (HY/T 0315-2021) [29], including range checks, correlation verification, temporal continuity analysis, and 3σ-based outlier detection. Records with H_s <0.1 m (attributed to non-physical wave states or instrument noise) were systematically excluded to ensure dataset robustness for statistical modeling.

Methods

The statistical analysis of wave data employed the zero up-crossing method to derive key parameters, including significant wave height (H_s), significant wave period (T_s), maximum wave height (H_{max}) with corresponding period (T_{max}), as well as mean wave height ($\bar{H}$) and period ($\bar{T}$).

The Fast Fourier Transform (FFT) method was used to estimate the wave energy spectrum, from which spectral parameters such as the significant wave height, the mean wave periods T_{01} and T_{02}, the spectral moments m_n (n = 0, 1, 2, …), and the spectral width parameters ε and ν were derived. Definitions of the wave parameters are as follows:

$$H_{m0} = 4\sqrt{m_0} \quad (1)$$

$$T_{01} = m_0/m_1 \quad (2)$$

$$T_{02} = \sqrt{\frac{m_0}{m_2}} \quad (3)$$

$$\varepsilon = \sqrt{1 - \frac{m_2^2}{m_0 m_4}} \quad (4)$$

$$\nu = \sqrt{\frac{m_0 m_2}{m_1^2} - 1} \quad (5)$$

$$m_n = \int_0^\infty f^n S(f) df, \mathrm{n} = 0, 1, 2, \ldots \quad (6)$$

where m_n is the n-th order spectral moment, f is the frequency, and $S(f)$ is the spectral energy density corresponding to f.

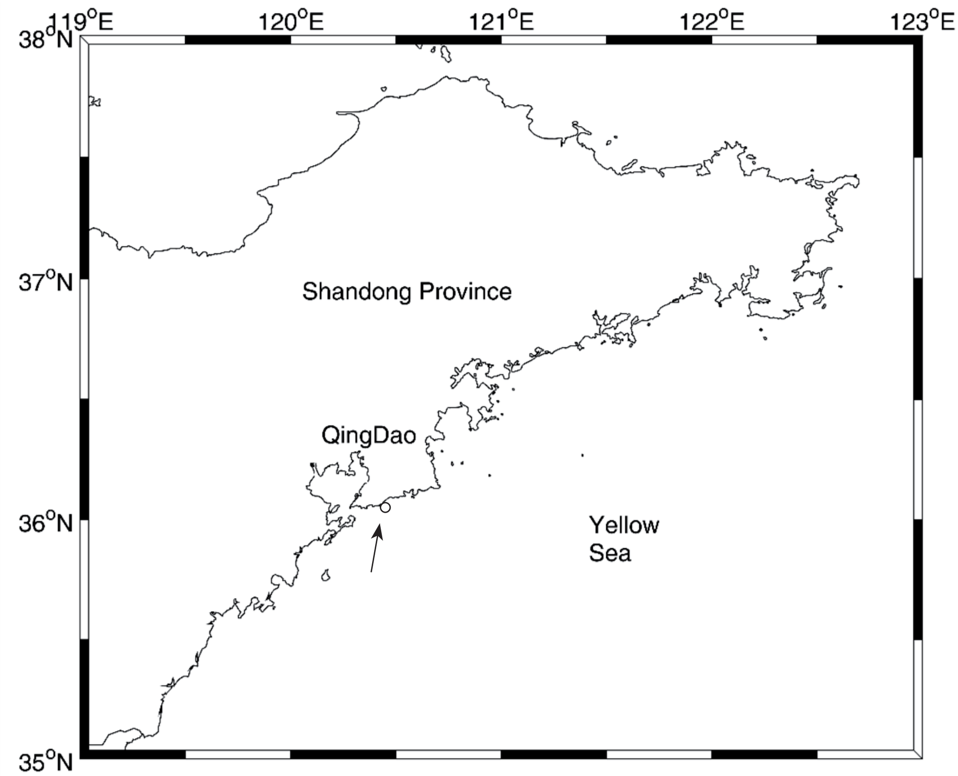

Fig. 1. Location of wave observation station (white dot, indicated by the arrow).

Table 1. Ranges and averages of various wave characteristic parameters from March 2020 to February 2021.

Month	H_{max}/m			H_s/m			$\bar{H}/s$		
	Range	Avg	Std	Range	Avg	Std	Range	Avg	Std
1	0.17~2.46	0.82	0.48	0.13~1.37	0.48	0.28	2.23~5.33	3.72	0.63
2	0.29~2.83	1.11	0.47	0.18~1.36	0.64	0.27	2.28~6.48	4.03	0.76
3	0.18~3.00	0.89	0.50	0.12~1.53	0.51	0.28	1.96~5.24	3.62	0.65
4	0.21~2.74	0.77	0.45	0.12~1.52	0.44	0.26	1.87~5.91	3.43	0.70
5	0.31~4.04	1.07	0.55	0.19~2.35	0.62	0.32	2.28~6.89	4.11	0.76
6	0.31~3.88	0.98	0.52	0.19~2.33	0.55	0.31	2.42~6.71	4.13	0.78
7	0.25~4.90	1.00	0.72	0.15~2.78	0.58	0.43	2.32~6.50	3.99	0.83
8	0.28~3.48	1.20	0.48	0.17~1.88	0.70	0.28	2.52~8.58	4.35	0.97
9	0.19~2.32	0.86	0.36	0.12~1.39	0.50	0.20	2.18~8.60	3.88	0.84
10	0.21~2.09	0.64	0.32	0.13~1.12	0.37	0.19	2.19~5.64	3.54	0.55
11	0.18~3.78	0.73	0.52	0.12~2.20	0.42	0.30	2.18~6.66	3.70	0.68
12	0.17~2.46	0.57	0.38	0.11~1.44	0.33	0.22	2.17~4.83	3.49	0.51
Total	0.17~4.90	0.88	0.52	0.11~2.78	0.51	0.31	1.87~8.60	3.83	0.79

Results and Discussion

Characteristics of Wave Distribution

In deep-water conditions, wave heights theoretically follow the Rayleigh distribution [30]:

$$f(H) = \frac{\pi}{2}\frac{H}{\bar{H}^2} exp\left[-\frac{\pi}{4}\left(\frac{H}{\bar{H}}\right)^2\right] \tag{7}$$

where H denotes individual wave height, and $\bar{H}$ represents the averaged wave height. While effective for linear waves with narrow-band spectra in deep water, this distribution deviates from observed patterns in shallow-water regimes.

Forristall [31] demonstrated the superiority of the two-parameter Weibull distribution through Gulf of Mexico observations:

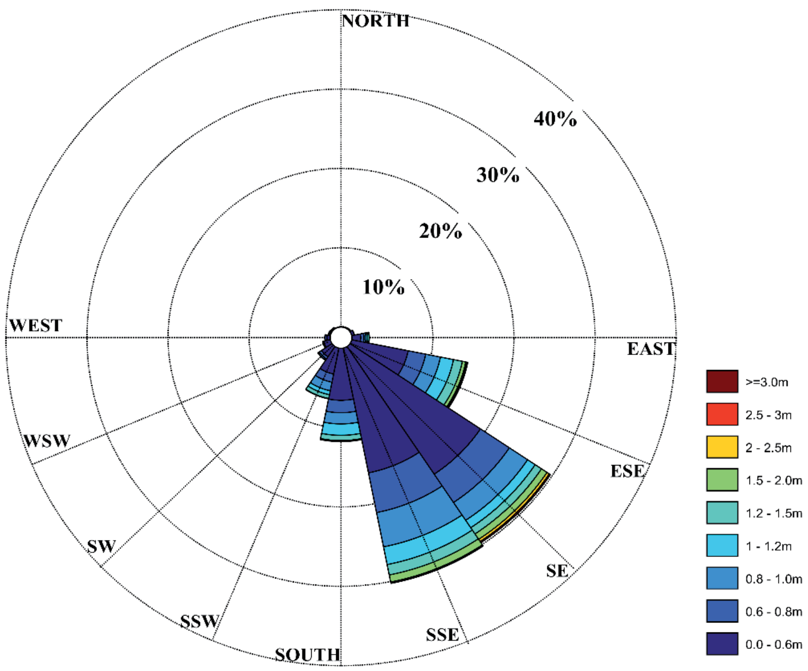

Fig. 2. Distribution of $H_{1/10}$ in different levels and different directions.

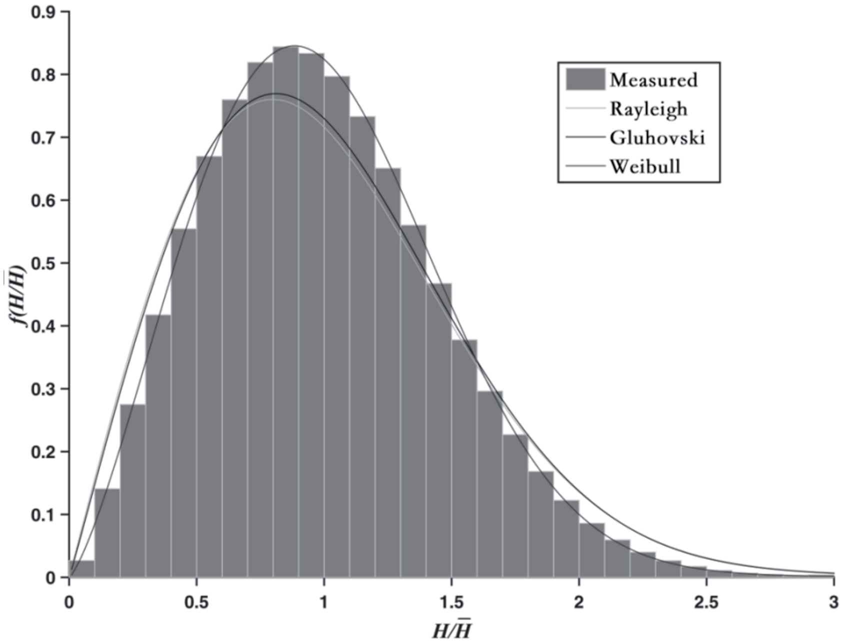

Fig. 3. Histogram and theoretical distributions of wave heights.

$$f(H) = \alpha\beta\left(\frac{H}{\overline{H}}\right)^{\alpha-1} exp\left[-\beta\left(\frac{H}{\overline{H}}\right)^{\alpha}\right] \quad (8)$$

where α and β are empirical coefficients determined from field data.

Incorporating bathymetric effects, Gluhovskiy [32] proposed a depth-modified formulation:

$$f(H) = \frac{\pi}{2\overline{H}(1-H^*)(1+0.4H^*)}\left(\frac{H}{\overline{H}}\right)^{\frac{1+H^*}{1-H^*}} \times exp\left[-\frac{\pi}{4(1+0.4H^*)}\left(\frac{H}{\overline{H}}\right)^{\frac{2}{1-H^*}}\right] \quad (9)$$

where the shallow-water parameter $H^* = \overline{H}/d$ (with d being the water depth) quantifies depth-limited wave transformation.

This study conducted a statistical analysis using one-year wave observation data (Table 1), obtaining probability histograms of wave height distribution and plotting probability density curves of the theoretical distributions mentioned above, as shown in Fig. 3. The results indicate that most wave heights are concentrated within twice the averaged wave height ($\overline{H}$), with the highest probability of occurrence observed at 0.8 to 0.9 times $\overline{H}$. Discrepancies exist between the Rayleigh distribution, Gluhovskiy distribution, and the measured histogram: both theoretical models overestimate the probability density in low wave height ratios ($H/\overline{H}<0.6$), underestimate probabilities near the peak region ($0.6<H/\overline{H}<1.5$), and overestimate probabilities in high wave height ratios ($H/\overline{H}>1.5$). The two-parameter Weibull distribution demonstrates the best fitting performance, effectively reflecting both the distribution pattern and numerical characteristics of wave height probability density in the Qingdao offshore area. The fitted parameters α and β are 2.32 and 1.32, respectively. Similar findings have been reported based on field observations in the Northern Yellow Sea, where Weibull distribution provides a more accurate representation of wave height probability characteristics compared with traditional Rayleigh assumptions [33].

Beyond probabilistic distributions of wave height, engineering applications frequently employ characteristic wave heights (Table 2), including the significant wave height (H_s), the averaged wave height ($\overline{H}$), and the maximum wave height (H_{max}). Establishing empirical relationships among these parameters enables mutual estimation, which holds both theoretical and operational importance for coastal engineering.

Using least squares regression on wave observations, we derived the following linear relationships (Fig. 4). Statistical results demonstrate strong correlations between $\overline{H}$ and H_s (correlation coefficient: 0.99), and between H_s and H_{max} (correlation coefficient: 0.98). The observed $H_s/\overline{H}$ ratio of 1.523 deviates from Longuet-Higgins' reported value of 1.598, and is lower than Yang's reported value of 1.58 in the central Hangzhou Bay. Similarly, the measured H_{max}/H_s ratio of 1.719 exceeds Longuet-Higgins' reported value of 1.628, but remains below Goda's [34] proposed value of 1.8 for vertical breakwater design. These discrepancies arise because the theoretical relationships are derived from deep-water wind-wave data, whereas the study area exhibits mixed wave conditions (containing both wind-generated waves and swells) typical of a coastal environment, thereby altering characteristic parameter ratios compared to theoretical expectations.

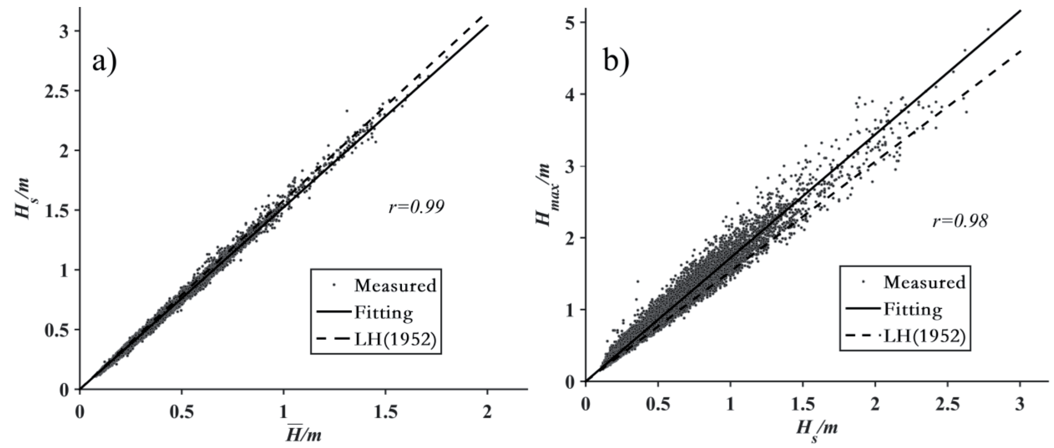

Fig. 4. Linear regressions between a) H and H_s, b) dimensionless H_s and H_{max}.

Table 2. Occurrence frequency of H_s categories.

H_s/m	Month												Total
	1	2	3	4	5	6	7	8	9	10	11	12	
0.1~0.5	65.7	34.6	57.9	70.1	42.1	54.0	62.1	22.8	55.9	83.1	77.7	82.1	59.0
0.5~1.0	27.1	53.3	35.8	24.7	45.9	37.8	25.7	66.8	42.6	15.7	17.7	16.1	34.1
1.0~1.5	7.1	12.1	6.1	5.1	9.7	6.8	6.7	8.2	1.5	1.2	2.5	1.8	5.7
>1.5	0	0	0.2	0.1	2.2	1.5	5.6	2.2	0	0	2.1	0	1.2

Table 3. Distribution of $H_{1/10}$ in different directions and different levels.

$H_{1/10}$ range (m)	Wave direction																
	N	NNE	NE	ENE	E	ESE	SE	SSE	S	SSW	SW	WSW	W	WNW	NW	NNW	Total
0.0~0.6	-	0.07	0.13	0.33	1.09	7.11	19.35	16.04	6.56	3.33	1.56	0.86	0.41	0.11	0.13	0.02	57.10
0.6~0.8	-	0.01	-	0.02	0.41	2.20	4.29	5.10	1.56	1.05	0.33	0.10	0.21	0.16	0.09	0.01	15.54
0.8~1.0	-	-	-	0.01	0.24	1.86	2.71	4.41	1.40	1.10	0.17	0.03	0.04	0.02	0.01	-	12.00
1.0~1.2	-	-	-	0.01	0.21	1.64	1.12	2.28	1.44	0.51	0.03	0.01	0.01	-	-	-	7.26
1.2~1.5	-	-	-	-	0.19	1.12	0.94	1.34	0.66	0.49	0.02	-	-	-	-	-	4.76
1.5~2.0	-	-	-	-	0.03	0.42	0.82	0.91	0.14	0.05	-	-	-	-	-	-	2.37
2.0~3.0	-	-	-	-	-	0.21	0.50	0.18	-	-	-	-	-	-	-	-	0.89
≥3.0	-	-	-	-	-	0.05	0.01	-	-	-	-	-	-	-	-	-	0.06
Total (%)	-	0.08	0.13	0.37	2.17	14.61	29.74	30.26	11.76	6.53	2.11	1.00	0.67	0.29	0.23	0.03	99.98
Average	-	0.44	0.39	0.41	0.68	0.72	0.59	0.65	0.64	0.65	0.50	0.46	0.56	0.60	0.55	0.46	0.64
Maximum	-	0.67	0.59	1.00	1.70	3.52	3.23	2.72	1.85	1.62	1.39	1.05	1.07	0.85	0.82	0.62	3.52

Systematic studies on wave period distributions emerged in the 1950s, yielding semi-empirical formulations. Gluhovskiy established a depth-independent period distribution for shallow waters:

$$f(T) = \frac{\pi}{1.2}\frac{T^3}{\overline{\overline{T}}^4} exp\left[-\frac{\pi}{4.8}\left(\frac{T}{\overline{\overline{T}}}\right)^4\right] \tag{10}$$

where T denotes the individual wave period and $\overline{T}$ represents the averaged period.

Sun [35] proposed another period distribution based on linear wave theory:

$$f(\tau) = \frac{1}{2\nu\tau}\left[1 + \frac{1}{\nu^2}\left(\frac{1}{\tau} - 1\right)^2\right]^{-\frac{3}{2}}$$

$$\times \left\{ 1 + \left[\frac{\nu^2 + \left(\frac{1}{\tau} - 1\right)^2}{\nu^2 + \left(\frac{1}{\tau} + 1\right)^2} \right]^{\frac{3}{2}} \right\} \tag{11}$$

where $\tau = T/\overline{T}$ is the dimensionless period.

The probability histogram of wave period distribution and corresponding theoretical density curves are shown in Fig. 5. Measured periods predominantly fall within 2.5 times the averaged period ($\overline{T}$), with peak probabilities occurring at τ = 1.0-1.1. Both the Gluhovskiy and Sun models overestimate maximum probabilities compared to observations. The Weibull distribution shows better agreement with observations, though it underestimates probabilities in the long-period region (τ>2.0). The fitted parameters are α = 2.90 and β = 0.80.

Similar to the analysis of characteristic wave heights, practical applications commonly use characteristic wave periods such as the significant wave period T_s, the averaged wave period $\overline{T}$, and the maximum wave period T_{max} to describe the statistical characteristics of wave periods in the offshore area. Analyzing the relationships between these characteristic periods holds significant importance in engineering.

The least squares method was employed to perform linear fitting on the relationships among common

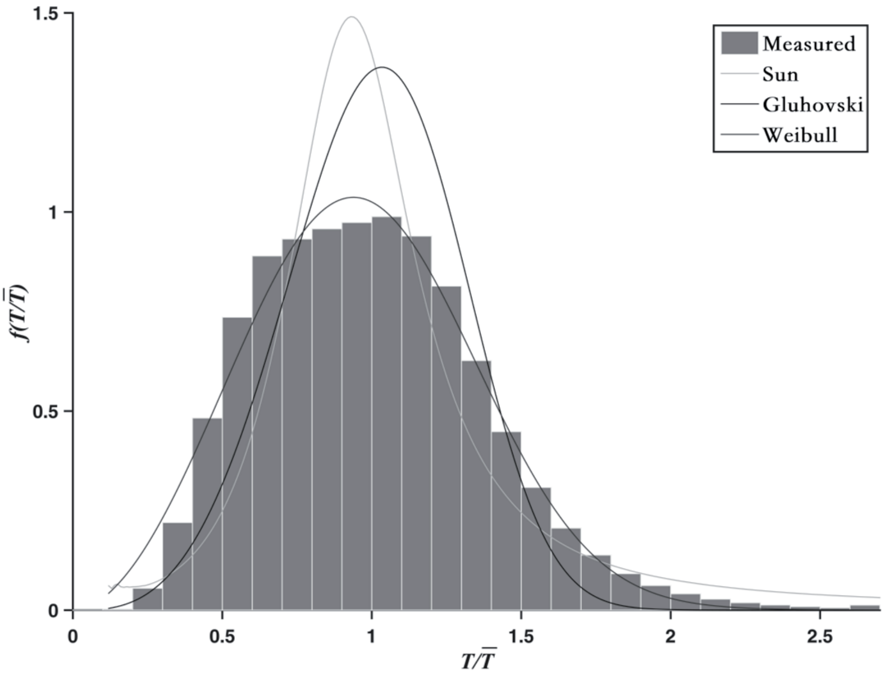

Fig. 5. Histogram and theoretical distributions of wave periods.

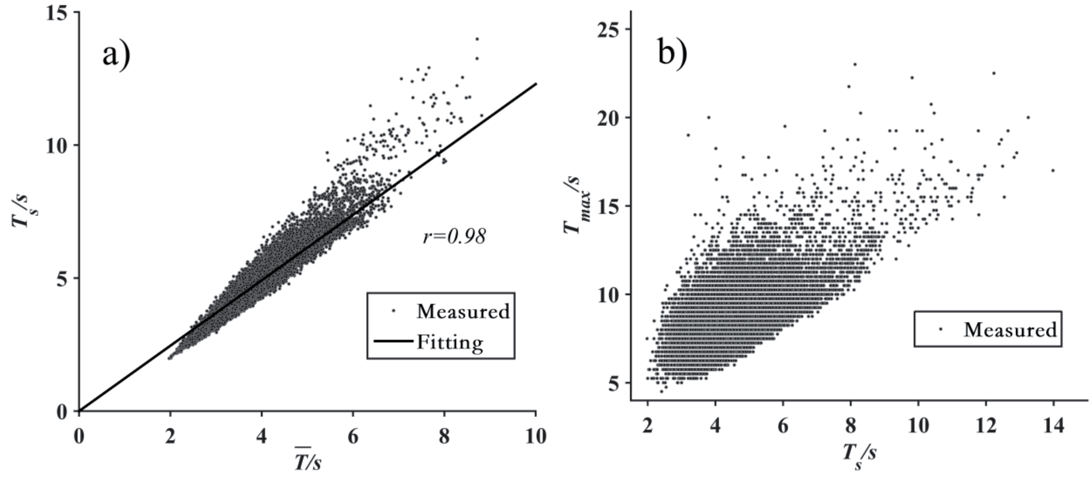

Fig. 6. Linear regressions between a) T and T_s, b) T_s and T_{max}.

characteristic wave periods, as shown in Fig. 6. Statistical results indicate a strong correlation between $\overline{T}$ and T_s, with a correlation coefficient of 0.98, and $T_s/\overline{T}$ is 1.284. In contrast, the correlation between T_s and T_{max} is relatively weaker, with a correlation coefficient of 0.65.

In addition to the individual distribution characteristics of wave height and period, researchers have conducted in-depth studies on the joint distribution of wave height and period. Currently, there exist several theoretically derived joint probability distribution functions for wave height and period. Sun [35] developed a joint distribution of wave height and period based on linear wave theory and wave ray theory. Building upon the aforementioned studies on wave height and period distributions, this work further analyses the joint distribution of wave height and period, with comparison against Sun's theoretical joint distribution, as shown in Fig. 7. The results indicate that the high-probability regions of the measured joint distribution (probability density >0.9) lie within wave height ratios of 0.3-1.0 and period ratios of 0.4-1.1. Overall, discrepancies exist between the measured joint distribution and Sun's theoretical model: while their contour patterns show similarity in low wave height ratios and low period ratios, the high-probability density region of the measured distribution shifts leftward compared to Sun's theoretical distribution, and the measured high-probability area covers a broader range than the theoretical prediction.

Characteristics of Wave Spectra

Wave spectra data corresponding to significant wave heights $H_s \geq 1$ were selected for analysis. Fig. 8 presents the monthly and seasonal averaged wave spectra (this study adopts the oceanographic definition of seasons: spring as April-June, summer as July-September, autumn as October-December, and winter as January-March).

Spectral analysis reveals that unimodal spectra dominate in most months. During spring and autumn, all monthly averaged spectra exhibit single peaks with spectral peak frequency concentrated between 0.1 and 0.2 Hz, indicating wind-dominated wave regimes. In summer, typhoon-induced swells propagating from the open ocean southwest of the Shandong Peninsula result in more complex spectral patterns: July shows a unimodal spectrum with the highest energy density, while August and September exhibit bimodal spectra. The primary peak (0.05-0.1 Hz) and secondary peak (0.1-0.2 Hz) in these bimodal spectra are attributed to swell and wind-wave frequency bands, respectively, suggesting a mixed sea state dominated by swells. Winter spectra display contrasting behaviours: January and March retain unimodal structures, whereas February shows a bimodal spectrum. The primary peak in February (~0.2 Hz) corresponds to locally generated wind-waves, while the secondary peak (~0.1 Hz) likely represents limited swells from cold surges. The suppression of swells is attributed to northerly wind directions and the blocking effect of the Shandong Peninsula, restricting fetch for swell development in the Qingdao offshore area.

Theoretically, the ratio of H_s to $m_0½$ (square root of the zeroth spectral moment) is approximately 4.0. However, real-world ocean waves are not narrow-banded. Fig. 9 illustrates the relationships between $\overline{H}$, H_s, and $m_0½$. The ratios are 2.471 and 3.764, respectively, slightly lower than the theoretical values of 2.5 and 4.0,

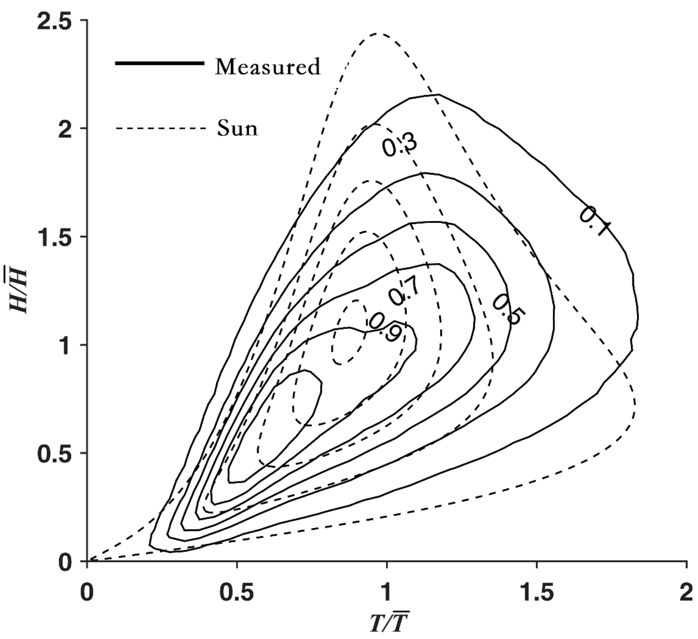

Fig. 7. Joint probability distributions of wave height and period.

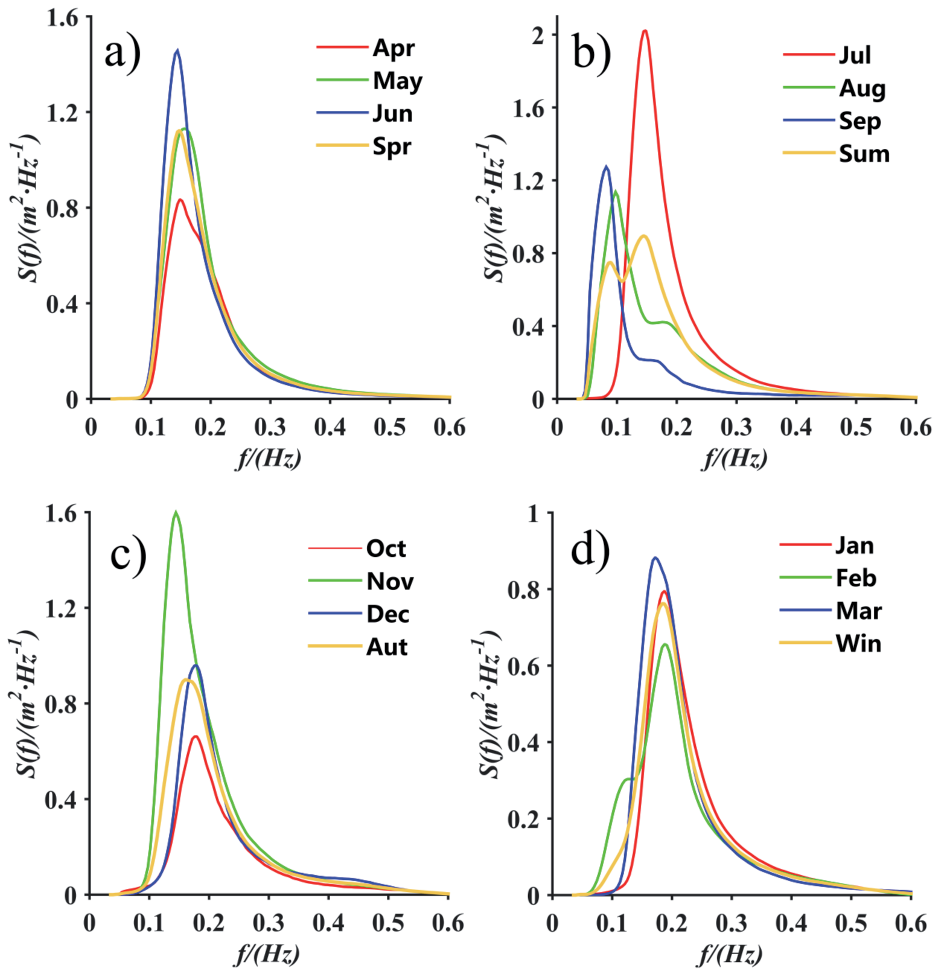

Fig. 8. Monthly and seasonal averaged wave spectra, a) spring, b) summer, c) autumn, d) winter.

indicating wave deformation caused by shallow-water effects at the observation site.

As mentioned above, we present two commonly used formulas for calculating wave periods from spectral moments. The relationships between the averaged wave periods T_{01} and T_{02} derived from these formulas and the significant wave period T_s obtained via the zero-crossing method are illustrated in Fig. 10. As shown, both T_{01} and T_{02} are smaller than T_s. The relationships between them are expressed as $T_s = 1.178T_{01}$ and $T_s = 1.293T_{02}$. Combined with the ratios between T_s and $\overline{T}$ mentioned above, $\overline{T} = 0.917T_{01}$ and $\overline{T} = 1.007T_{02}$, which differ from the deep-water condition where $\overline{T} \approx T_{01}$.

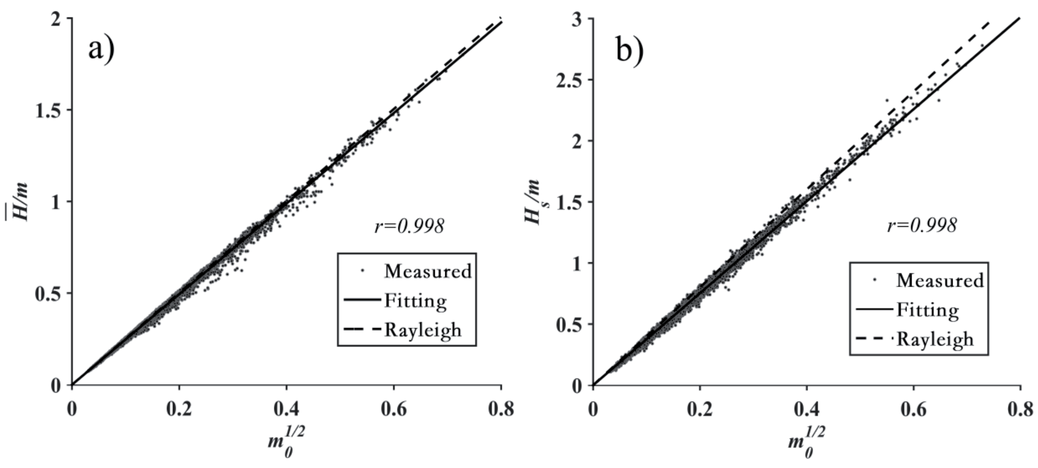

Fig. 9. Relationships between a) and H, b) and H_s.

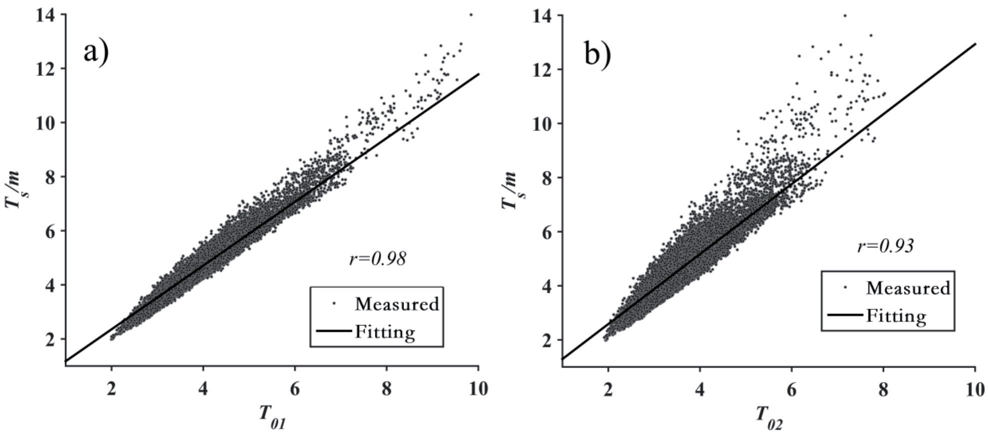

Fig. 10. Relationships between a) spectral T_{01} and T_s, b) spectral T_{02} and T_s.

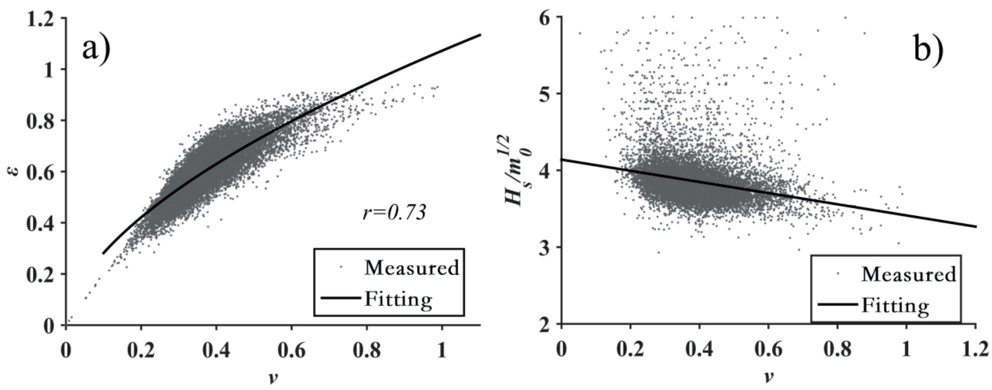

Fig. 11. Relationships between a) spectral bandwidth parameters ε and ν, b) dimensionless H_s/and ν.

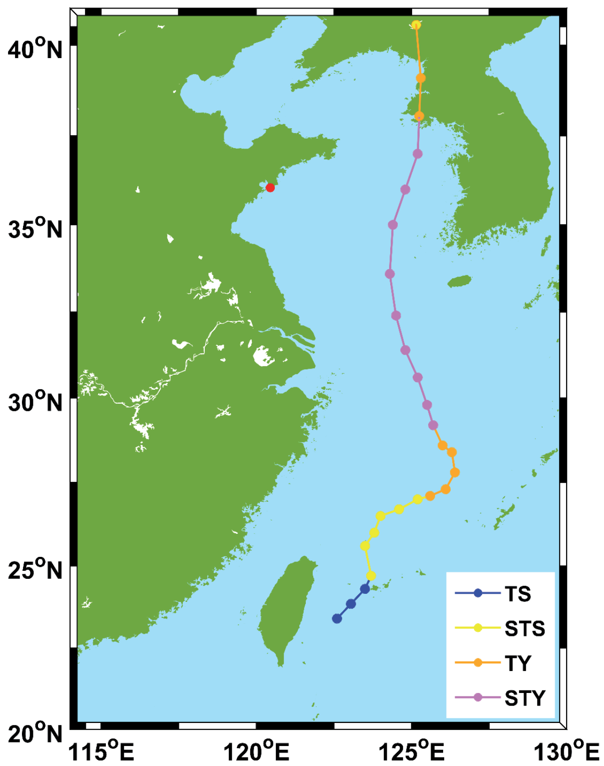

Fig. 12. Traveling path of Typhoon Bavi.

The spectral width parameters *ε* and *ν* were calculated using the formulas mentioned above to reflect the degree of energy concentration within the wave spectrum. For deep-water narrow-band waves, Longuet-Higgins derived the theoretical relationship between these parameters as $\varepsilon \approx 2\nu$. However, real ocean wave spectra are often non-narrow-band. In this study, the least squares method was applied to analyze the relationship between the two spectral width parameters in the study area. As shown in Fig. 11, the fitted relationship is $\varepsilon \approx 1.07\nu^{0.58}$.

Vandever [10] analyzed the relationship between *ν* and the dimensionless parameter H_s/m_0½, proposing the relationship H_s/m_0½ = 3.95 – 0.537*ν*. Under narrow-band conditions (*ν* = 0), this simplifies to H_s/m_0½ = 3.95, which closely aligns with the theoretical deep-water narrow-band value of 4.0. For the study area, the least squares fitting of measured data yields H_s/m_0½ = 4.14 – 0.727*ν*, shown in Fig. 10.

Wave Process during Typhoon Bavi

During 23-29 August 2020, Typhoon Bavi traversed the Yellow Sea and moved northward before landfall (Fig. 12), exerting a pronounced impact on wave conditions in Qingdao offshore waters. This study focuses on the wave evolution process induced by Typhoon Bavi (202008), which provides valuable insight into coastal engineering design and hazard mitigation. The observed wave evolution characteristics are consistent with previous spectral analyses of typhoon-induced wave systems in marginal seas [16, 25].

The dominant wind direction during Typhoon Bavi was northerly, rotating in accordance with the storm track (Fig. 13a)). Both the mean wave period ($\overline{T}$) and spectral peak period (T_p) exhibited an initial increase followed by a decrease, with the spectral peak period stabilizing around 12 s between 25-26 August (Fig. 13b)). This indicates that long-period swells dominated the wave field during the mature stage of the typhoon. After 11:00 on 25 August, the one-tenth wave height ($H_{1/10}$, Table 3) and wind increased significantly, and their temporal variations exhibited strong consistency (Fig. 13c)). This close correspondence reflects the dominant control of local wind forcing on nearshore wave growth during the peak stage of

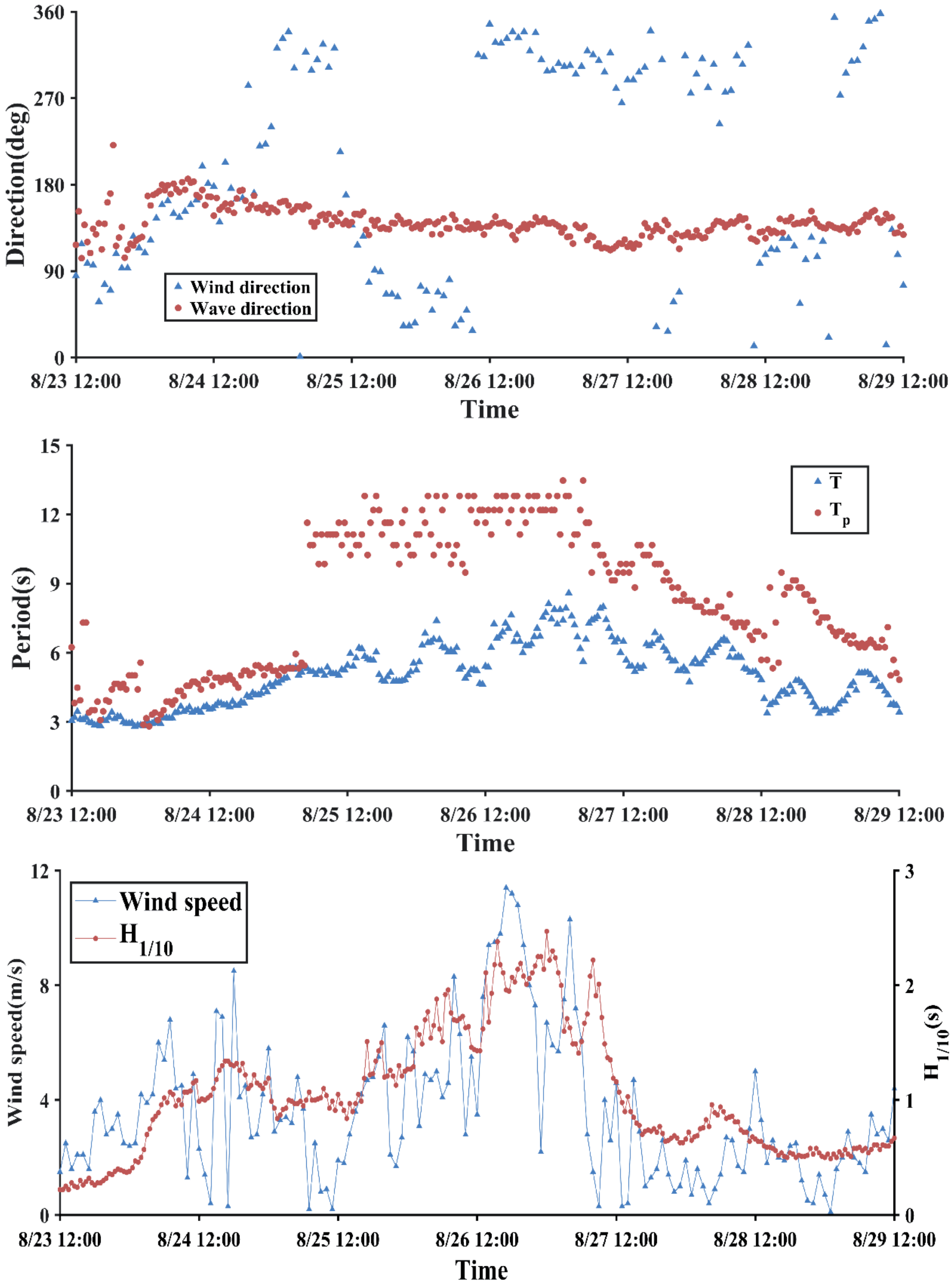

Fig. 13. Variations of wave parameters from 12:00 on 23 August to 12:00 on 29 August 2020 during Typhoon Bavi.

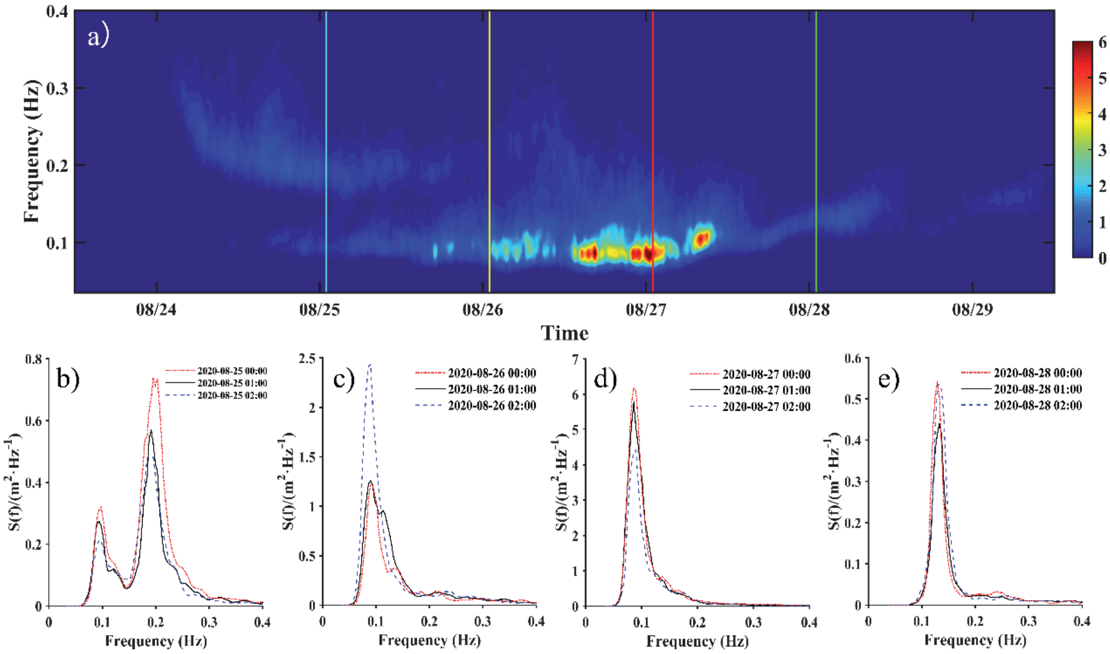

Fig. 14. Time series plot of the normalized spectral energy density with frequency during Typhoon Bavi.

the storm. Influenced by coastal topography, waves propagating from the southeast underwent refraction and diffraction before reaching the observation site, resulting in a strong positive correlation between wave height and wind speed, whereas wave direction exhibited partial decoupling from instantaneous wind direction.

To further investigate the energy distribution during the typhoon event, the normalized wave spectral energy density in the frequency–time domain was analyzed (Fig. 14). The high-wave process lasted approximately two days, during which wave spectra were predominantly single-peaked. Fig. 14(b-e) illustrate representative spectral snapshots corresponding to selected time intervals marked in Fig. 14a). The dominant energy was concentrated at low frequencies around 0.09 Hz, indicating swell-dominated conditions. The maximum wave height is marked by the red line in Fig. 14a), corresponding to a peak spectral energy density of approximately 6 m²/Hz at 0.09 Hz (Fig. 14d)).

Portilla et al. [36] proposed an algorithm for identifying wind-sea and swell components based on spectral peak energy. The parameter γ^* is defined as the ratio between the measured peak spectral energy and the energy of a Pierson–Moskowitz (PM) spectrum at the same peak frequency:

$$S(f_p) = \alpha g^2 (2\pi)^{-4} f_p^{-5} e^{-\frac{5}{4}} \tag{12}$$

where *S(f)* is the energy spectrum, *fp* is the peak frequency, α is the Phillips constant fixed to its PM value, and g is gravitational acceleration.

Calculated results show that the PM spectral energy at 0.09 Hz is 24.22 m²/Hz, whereas at 0.20 Hz it is 0.45 m²/Hz. Comparing these theoretical values with the measured spectral energy (Fig. 14(b-e) indicates that $\gamma^*<1$ in the low-frequency band (~0.09 Hz) and $\gamma^*>1$ in the higher-frequency band (~0.20 Hz). Therefore, the wave field during Typhoon Bavi was predominantly swell-dominated, with locally generated wind waves contributing secondary energy at higher frequencies.

Conclusions

(1) Pronounced seasonal variability characterizes the wave climate in the Qingdao offshore area, with extreme wave events primarily modulated by summer typhoons and winter cold surges.

(2) The two-parameter Weibull distribution demonstrates superior applicability for both wave height ($\alpha = 2.32$, $\beta = 1.32$) and wave period ($\alpha = 2.90$, $\beta = 0.80$) statistics, exhibiting correlation coefficients exceeding 0.98 for characteristic wave height relationships. The high-probability region of the measured joint wave height–period distribution occurs near normalized ratios of approximately 0.7 for both wave height and period, deviating from Sun's theoretical joint distribution pattern.

(3) Spectral analysis reveals distinct seasonal regimes. Wave spectra are predominantly unimodal in most months, with peak frequencies concentrated between 0.1 and 0.2 Hz during spring and autumn, indicating wind-dominated wave conditions. Under episodic extreme events such as summer typhoons and winter cold surges, bimodal spectra are observed in February, August, and September, representing mixed sea states consisting of swell and wind-sea components.

(4) Most wave parameters exhibit strong correlations. Due to shallow-water effects and mixed sea conditions, the ratios of characteristic wave heights (H and H_s) relative to √m0 are smaller than classical deep-water theoretical values. The relationships among wave periods indicate $T_s \approx 1.18T_{01}$ and $T_s \approx 1.29T_{02}$, deviating from theoretical deep-water expectations. Strong correlations are observed between spectral width parameters ε and ν, with the fitted relationship $\varepsilon \approx 1.07\nu^{0.58}$. A negative correlation exists between the dimensionless parameter Hs/√m0 and ν, expressed as $H_s/m_0½ = 4.14 - 0.727\nu$.

(5) Qingdao was affected by Typhoon Bavi for approximately two days. During the typhoon period, wave height exhibited a strong positive correlation with wind speed, whereas wave direction showed partial decoupling from instantaneous wind direction. The averaged wave direction primarily reflected long-period swells propagating from the open Yellow Sea. Spectral analyses indicate that wave spectra predominantly exhibited single-peaked structures with dominant low-frequency energy, and wind-sea-swell identification confirms that swell components dominated the wave field during Typhoon Bavi.

Acknowledgements

The project was supported by the Fund of Key Laboratory of Ecological Prewarning, Protection and Restoration of Bohai Sea, Ministry of Natural Resources, No.2026203. And the Open Fund Project of the Key Laboratory of Ocean Observation Technology, No.2025KLOOTA01.

AI Usage Disclosure Statement

During the preparation of this work, the author used ChatGPT solely for the purpose of translating and polishing specific sections of the manuscript (primarily the Abstract, Introduction, and Conclusion) from Chinese to English, in order to improve readability and academic tone. After using this tool, the author carefully reviewed and edited the content as needed and takes full responsibility for the final content of the published article.

Conflict of Interest

The authors declare no conflict of interest.

References

1. INTERGOVERNMENTAL PANEL ON CLIMATE CHANGE (IPCC). Climate Change 2021: The Physical Science Basis; Cambridge University Press: Cambridge, **2021**.
2. KLOTZBACH P.J., WOOD K.M., SCHRECK C.J., BOWEN S.G., PATRICOLA C.M., BELL M.M. Trends in global tropical cyclone activity: 1990–2021. Geophysical Research Letters, **49** (6), e2021GL095774, **2022**.
3. LOBETO H., SEMEDO A., LEMOS G., DASTGHEIB A., MENENDEZ M., RANASINGHE R., BIDLOT J.-R. Global coastal wave storminess. Scientific Reports, **14** (1), 3726, **2024**.
4. BOOIJ N., HOLTHUIJSEN L.H., RIS R.C. The SWAN wave model for shallow water. Coastal Engineering, **53**, 668, **1996**.
5. AYDOĞAN B., AYAT B. Performance evaluation of SWAN ST6 physics forced by ERA5 wind fields for wave prediction in an enclosed basin. Ocean Engineering, **240**, 109936, **2021**.
6. MENG Y., LIANG B., GAO H., SHAO Z. Analysis and extreme event prediction of waves in the eastern shelf seas of China based on a 44-year hindcast. Ocean Engineering, **312**, 119102, **2024**.
7. WAVEWATCH III DEVELOPMENT GROUP (WW3DG). User manual and system documentation of WAVEWATCH III version 6.07; NOAA/NWS/NCEP/MMAB Tech. Note 333, **2019**.
8. AMAROUCHE K., AKPINAR A., RYBALKO A., MYSLENKOV S. Assessment of SWAN and WAVEWATCH-III models regarding the directional wave spectra estimates based on Eastern Black Sea measurements. Ocean Engineering, **272**, 113944, **2023**.
9. YAO R., SHAO W., ZHANG Y., WEI M., HU S., ZUO J. Feasibility of wave simulation in typhoon using WAVEWATCH-III forced by remote-sensed wind. Journal of Marine Science and Engineering, **11** (10), 2010, **2023**.
10. VANDEVER J., SIEGEL E., BRUBAKER J.M., FRIEDRICHS C.T. Influence of spectral width on wave height parameter estimates in coastal environments. Journal of Waterway, Port, Coastal, and Ocean Engineering, **134** (3), 187, **2008**.
11. BACK J.-D., CHANG Y.S., RYU K.H., CHO H.Y., CHOI H.J., JEONG W.M. Revised system for shallow-water design wave estimation on the coast of the Republic of Korea based on numerical model data. Ocean and Coastal Management, **244**, 106777, **2023**.
12. LI R., WU K., LI J., DONG X., SUN J., ZHANG W., LIU Q. Relating a large-scale variation of waves in the Indian Ocean to the Indian Ocean Dipole. Journal of Geophysical Research: Oceans, **127**, e2022JC018941, **2022**.
13. PORTILLA-YANDÚN J. The world ocean wave fields discerned from ERA-Interim spectra. Journal of Geophysical Research: Oceans, **127**, e2022JC018775, **2022**.
14. KUMAR V.S., MANDAL S. Characteristics of individual surface waves measured by moored buoys in the coastal waters of the eastern Arabian Sea. Ocean Engineering, **248**, 110861, **2022**.
15. GAO X., MA X., MA Y., HUANG X., ZHENG Z., DONG G. Spectral characteristics of swell-dominated seas with in situ measurements in the coastal seas of Peru and Sri Lanka. Journal of Atmospheric and Oceanic Technology, **39** (6), 755, **2022**.
16. PENG J., MAO M., XIA M. Wave spectra analysis on the spatiotemporal variability of sea states under distinct typhoon tracks in a semi-enclosed sea. Journal of Physical Oceanography, **54** (3), 783, **2024**.
17. RAJ A., KUMAR P., JAMPANA V., REMYA P.G., SEO H., SURESHKUMAR N., RAO E.P.R. Wind-stress misalignment in the presence of swells in the Bay of Bengal. Frontiers in Marine Science, 12, **2025**.

18. LIU X., CHEN W., SUN Z., CAI Z., HOU Y. Investigation on the reconstruction of wave bimodal spectrum in the lagoon near islands and reefs. Ocean Engineering, 265, 112615, **2022**.
19. MIAO Q., YANG J., WANG Z., ZHANG Y., YANG Y., WEI G., DING F., CHENG L. A study on wave climate variability along the nearshore regions of Bohai Sea based on long-term observation data. Ocean Engineering, **304**, 117947, **2024**.
20. ZHOU Y., LI Z., PAN Y., BAI X., WEI D. Distribution characteristics of waves in Sanmen Bay based on field observation. Ocean Engineering, **229**, 108999, **2021**.
21. WANG Z., CHEN Y., LIU L., YUAN H., ZOU L. Current effect on wave condition around island in the South China Sea. Journal of Atmospheric and Oceanic Technology, **40** (10), 1307, **2023**.
22. MA Y., WU Y., SHAO Z., CAO T., LIANG B. Impacts of sea level rise and typhoon intensity on storm surges and waves around the coastal area of Qingdao. Ocean Engineering, **249**, 110953, **2022**.
23. ZHOU C.-Y., ZHANG M.-Z., XU C.-Y., WANG P., GUO Y.-K. Effects of radial sand ridges on storm surge under different extreme weather events in the South Yellow Sea. China Ocean Engineering, **39**, 1139, **2025**.
24. LI D., FENG J., ZHU Y., STANEVA J., QI J., BEHRENS A., LEE D., MIN S.-K., YIN B. Dynamical projections of the mean and extreme wave climate over the Bohai Sea, Yellow Sea, and East China Sea. Frontiers in Marine Science, **9**, 844113, **2022**.
25. YANG Z., YE Q., YANG B., SHI W., ZHANG J. Characteristics of measured typhoon waves on the central coast of Zhejiang Province. Frontiers in Marine Science, **11**, 1494107, **2024**.
26. JIA L., WU S., HAN B., CAI S., WU R. Wave hindcast under tropical cyclone conditions in the South China Sea: sensitivity to wind fields. Acta Oceanologica Sinica, **42**, 36, **2023**.
27. ZHANG S., YANG Z., ZHANG Y., ZHAO S., WU J., WANG C., WANG Y.-G., JENG D.-S., NIELSEN P., LI G., LI S. Improved prediction of local significant wave height by Considering the Memory of Past Winds Water Resources Research, **59** (8), **2023**.
28. WINKLERPRINS L., LARGIER J.L., VILA-CONCEJO A., GALLOP S.L., FELLOWES T.E., RAHBANI M. Components and tidal modulation of the wave field in a semi-enclosed shallow bay. Estuaries and Coasts, **46**, 645, **2023**.
29. MINISTRY OF NATURAL RESOURCES OF THE PEOPLE'S REPUBLIC OF CHINA. Technical specification for delayed-mode ocean observation data quality control and check; Beijing, **2021**.
30. LONGUET-HIGGINS M.S. On the statistical distribution of the height of sea waves. Journal of Marine Research, **11** (3), 245, **1952**.
31. FORRISTALL G.Z. On the statistical distribution of wave heights in a storm. Journal of Geophysical Research, **83** (C5), 2353, **1978**.
32. GLUHOVSKIY B.H. Distribution characteristics of wave parameters and changes in wave action with depth. Report of State Institute of Oceanology, Moscow, 93, 98, **1968**.
33. SHI H., XUE H., LI L., ZHAN C., YOU Z. Analysis of wave characteristics in the Northern Yellow Sea based on field observations. Applied Ocean Research, **158**, 104527, **2025**.
34. GODA Y. Random Seas and Design of Maritime Structures, 2nd Ed.; World Scientific: Singapore, pp. 464, **2000**.
35. SUN F. The joint distribution of sea wave period and wave height. Acta Oceanologica Sinica, **10** (1), 10, **1988** [In Chinese].
36. PORTILLA J., OCAMPO-TORRES F.J., MONBALIU J. Spectral partitioning and identification of wind sea and swell. Journal of Atmospheric and Oceanic Technology, **26** (1), 107, **2009**.